Needle Insertion Parameter Optimization for Brachytherapy

Ehsan Dehghan, *Student Member, IEEE*, and Septimiu E. Salcudean, *Fellow, IEEE*

Abstract—This paper presents a new needle path planning method for the insertion of rigid needles into deformable tissue. The needle insertion point, needle heading, and needle depth are optimized by minimizing the distance between a rigid needle and a number of targets in the tissue. The optimization method is based on iterative simulations performed using a tissue finite element model. At each iteration, the best 3-D line fitted to the displaced targets in the deformed tissue is used as a candidate for a new insertion line. First, this method is implemented in a prostate brachytherapy simulator under different boundary conditions to minimize the targeting error. It is shown that the optimization method converges in a few iterations and decreases the seed misplacement error to less than the needle diameter. Second, the efficacy of the optimization algorithm is verified by optimizing the insertion parameters for a brachytherapy needle before insertion into a prostate tissue phantom. The elastic properties of the phantom and the needle–tissue interaction parameters were identified in an independent experiment. The optimization algorithm is effective in decreasing the targeting error.

Index Terms—Brachytherapy, Finite Element Method (FEM), needle insertion, needle path planning.

I. INTRODUCTION

NEEDLE insertion is involved in many medical interventions. In spite of the use of image guidance, accurate needle placement is still a challenge in many procedures. One example illustrating the need for accurate placement is low-dose-rate prostate brachytherapy. This effective treatment for localized prostate cancer consists of implanting many tiny radioactive capsules or "seeds" of ^{125}I or ^{103}Pd inside the prostate and the periprostatic tissue using long needles (see Fig. 1). In order to kill the cancerous tissue while maintaining a tolerable radiation dose on other organs, the seed distribution is carefully planned prior to the intervention using brachytherapy treatment planning software. The planning software requires a 3-D prostate model, typically constructed from several parallel transversal transrectal ultrasound (TRUS) images that are manually segmented. This 3-D model is used to plan for the seed positions that are usually along straight lines parallel to the long axis of
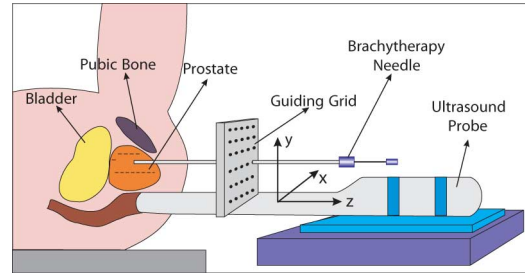

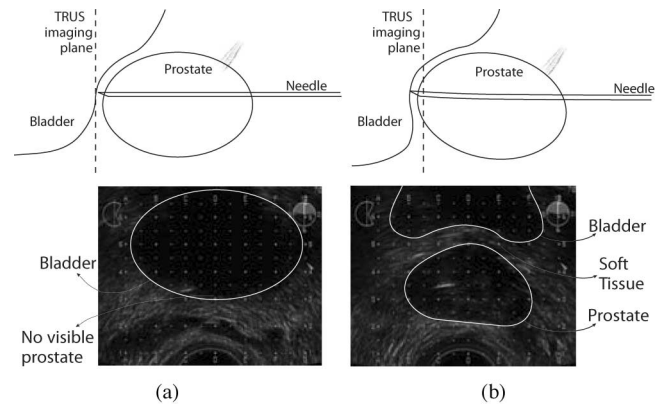Fig. 1. Insertion of the needle during prostate brachytherapy.

Fig. 2. Prostate displacement during needle insertion. The image is taken from [3].

the ultrasound (US) probe (the z-axis in Fig. 1). In the operating room, the physician registers the real-time TRUS images of the prostate to the preoperatively acquired images used for planning and then implants the seeds, typically using preloaded needles. To deliver the seeds according to the plan, the physician inserts the needle through a guiding template—a grid with equidistant 5-mm-apart parallel guidance holes in the x–y plane. The grid confines the needle movement along the z-axis. Real-time US and occasional X-ray fluoroscopy are used for visual feedback during the operation.

During the insertion, the prostate moves and deforms due to needle forces. The rotation is caused by the configuration of boundary conditions (pubic arch, bladder) and tissue deformation parameters and likely by a stiffer anterior anchoring of the prostate to the pubic arch. The prostate displacement during needle insertion is illustrated in Fig. 2 using US images of the region in the transverse view. At first, only the bladder can be seen in the US image as in Fig. 2(a). When the needle penetrates more into the prostate, it pushes the prostate back into the bladder; hence, in Fig. 2(b), the prostate and the needle tip are visible in the US image. Lagerburg *et al.* measured the rotation of the

The authors are with the Department of Electrical and Computer Engineering, University of British Columbia, Vancouver, BC V6T 1Z4, Canada (e-mail: ehsand@ece.ubc.ca; tims@ece.ubc.ca).

prostate during brachytherapy and found it to be significant, often in excess of 10° [1]. As a result of prostate motion, seed misplacements are still common in brachytherapy [2]. Misplacements can lead to underdosed regions that may require repeated treatment or to higher doses that can cause complications—such as impotence or urinary incontinence.

The guiding template allows the needle to move along the z-axis only. However, the target positions diverge from this line during insertion due to tissue deformation. Modeling the tissue deformation and allowing for an arbitrary needle insertion direction as opposed to only parallel directions may allow for more accurate delivery of seeds.

A number of brachytherapy robots have been developed (e.g., [4]–[9]) that are able to insert the needle with desired preplanned orientation. However, the problems of preplanning for brachytherapy in the presence of tissue deformation and path planning for brachytherapy robots have not been solved. A few methods have been introduced to optimize the needle insertion depth, initial position, and/or orientation for 2-D deformable tissue models with single targets [10], [11]. However, no method has been reported previously for insertion point and heading optimization for needle path planning in 3-D and in the presence of multiple targets.

This paper proposes such a method, based on 3-D simulations that use the finite element method (FEM). The paper is organized as follows. An overview of the previous research on needle insertion is presented in Section II; the details of the optimization method are described in Section III, followed by the description of the simulation method in Section IV. Needle insertion planning simulation results for a brachytherapy simulation and experimental validation on a tissue phantom are presented in Sections V and VI, respectively, followed by a discussion in Section VII. Conclusions and future research are presented in Section VIII.

II. RELATED WORK

Needle insertion into soft tissue has been a topic of many research activities in the past decade (for a survey please see [12]). Among different methods available, the FEM—a powerful approximate solution to solid mechanics problems—has been widely used to simulate tissue deformation during surgery and needle insertion [10], [13]–[16]. Alterovitz et al. [15] simulated brachytherapy using a 2-D linear FEM-based model. Goksel et al. [3], [14] generated a 3-D mesh of the prostate—constructed from manually segmented transverse images—and used it in a 3-D brachytherapy simulator. Computation acceleration techniques have been presented for 2-D and 3-D linear FEM-based needle insertion models to achieve high speeds [13], [14].

Alterovitz et al. optimized the needle insertion height and depth to decrease the seed misplacement error for a single target, in a 2-D brachytherapy simulator [10]. They used a search-based algorithm to optimize the two parameters. For optimization of the insertion depth, they simulated the insertion of a needle with a given insertion height to the maximum depth allowed. The optimal depth for the given height is the depth with minimum error. To optimize the insertion height, they used the

golden section search method. Extension of this method to 3-D will result in a system with three more optimization parameters (width of the insertion point and two angles for needle orientation). Optimizing for these parameters using a search-based algorithm requires a large number of simulations. In another study, Alterovitz et al. optimized the initial point and angle for insertion of a highly flexible needle into a 2-D tissue to reach a target while avoiding obstacles [11]. Their technique involves the transformation of the constrained optimization problem into an unconstrained one using a penalty method, then applying a gradient descent algorithm to solve the problem. Due to its complexity, the cost function cannot be directly differentiated with present techniques. Therefore, the authors used a perturbation method to find the approximate derivatives of the cost function at each iteration, each requiring multiple simulations. As opposed to these gradient-based approaches, the algorithm presented in this paper does not need the derivatives of the cost function and addresses the 3-D problem. An average plan for prostate brachytherapy treatment involves 20–30 needle insertions. The planning algorithm can be used preoperatively to optimize the insertion parameters in order to achieve accurate implants. Furthermore, a number of studies have shown that there may be a benefit in terms of improved outcomes from the simultaneous planning and execution of needle insertions intraoperatively, as a function of intraoperatively computed dose computations [17]. Thus, the need for high-speed planning is clear.

The needle model used in [11] is a nonholonomic model fitted to a highly flexible bevel-tip needle by Webster et al. [18]. Alterovitz et al. [19] used the same needle model to steer the needle tip inside a 2-D tissue model under Markov uncertainty. They used the needle bevel-tip direction as input and guided the needle to reach a target while avoiding obstacles. However, they did not optimize the initial needle position or orientation. Park et al. formulated the problem of steering a highly flexible needle as a nonholonomic kinematics problem and addressed the planning problem by diffusion-based motion planning on the Euclidean group, SE(3) [20]. However, they did not simulate the tissue deformation caused by insertion forces. The highly flexible needle model, which assumes the needle follows its beveled tip trajectory direction without applying considerable lateral force to the tissue is not applicable to brachytherapy needles. In [21], three different models for brachytherapy needles were compared.

DiMaio and Salcudean used a 2-D nonlinear FEM-based model for the needle and manipulated the needle base to steer the tip inside tissue [22]. They related the movements of the needle tip to the movements of the base using a numerically computed needle Jacobian. They steered the flexible needle to hit a target while avoiding obstacles using potential fields. Using a spring mesh for the tissue and a linear beam model for the needle, Glozman and Shoham steered a needle inside the tissue by using the inverse kinematics of the needle [23]. The initial location and orientation of the needle were not optimized in [22] or [23].

Needle rotation and insertion speed were used to reduce tissue deformation during insertion as in [24] and [25]. Heverly et al. [25] showed that velocity-dependent properties of the tissue can

be used to reduce tissue deformations at high needle insertion speed, essentially hammering the needle into prostate.

In contrast to other published research, this paper proposes a method to optimize the needle insertion point and heading into a 3-D tissue model containing multiple targets. The presented method, which, for now, assumes a rigid needle, uses the simulation results to modify the insertion parameters.

To simulate the tissue deformation as a result of needle insertion, in addition to a model for the tissue, a model for needle–tissue interaction needs to be developed. Okamura *et al.* [26] divided the forces applied by the needle into three parts: 1) a force due to capsule stiffness occurring before puncture of the capsule; 2) a friction force acting on the needle shaft; and 3) a cutting force on the needle tip. They modeled the capsule stiffness force with a nonlinear spring, the friction force with a modified Karnopp model, and the cutting force with a constant for a given tissue. DiMaio and Salcudean [13] introduced the stick–slip needle–tissue interaction model, based on the force measurements during insertion of a needle into a slab of polyvinyl chloride (PVC). They used this model to accurately predict insertion trajectories in PVC phantoms, and also to achieve high computational speed. Dehghan *et al.* [27] introduced a three-parameter force model based on the experimental data during insertion of a brachytherapy needle into a nonhomogeneous prostate phantom. Kataoka *et al.* [28] measured the force applied to a needle during insertion into a canine prostate. Needle motion and forces during brachytherapy of several patients were reported by Podder *et al.* in [29].

III. OPTIMIZATION METHOD

As done in prior studies—see, for example, [10] and [30]—the optimization method in this paper is based on simulations. In each iteration of the optimization, the simulation program finds the location of the displaced targets after the deformation caused by needle insertion with given initial orientation, tip location, and depth. Therefore, the simulation acts as a function in which the needle insertion point p_s, needle heading—shown as a unit vector v—and needle insertion depth d are the input parameters and the target displaced positions are the outputs. Other parameters such as tissue elasticity parameters, target initial positions, and needle–tissue interaction parameters are assumed to be known constants in this function. Assuming N targets located in the tissue, the input–output relation can be written as

$$u_i = \mathcal{F}_i(p_s, v, d), \qquad i \in \{1, 2, \ldots, N\} \tag{1}$$

where u_i are the displaced locations of the targets (u_N is the displaced position of the distal target). The optimization goal is to minimize the distance between a rigid needle and the displaced targets in the deformed configuration, by optimizing the needle insertion point, heading, and depth, i.e.

$$(p_s^*, v^*, d^*) = \arg\min_{p_s, v, d} \left(\sum_{i=1}^{N} \min_{\alpha} \|p_s + \alpha v - u_i\|^2 \right)$$

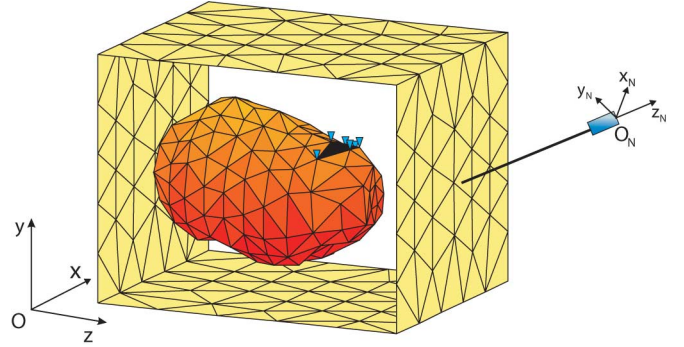$$\text{subject to} \quad u_i = \mathcal{F}_i(p_s, v, d), \quad \alpha \le d, \quad \|v\| = 1. \tag{2}$$

Fig. 3. Simplified mesh of prostate and surrounding tissue. The area connected to the pubic bone is shown in black color.

The constraint $\alpha \le d$ assures that for the targets deeper than the needle tip, the cost function is calculated as the distance of these targets from the needle tip. Assume a global coordinate system $Oxyz$ and a needle-attached coordinate system $O_N x_N y_N z_N$ as shown in Fig. 3. Since the needle is axially symmetric, the pitch and yaw angles are sufficient to relate the bases of two coordinate systems. Therefore, the two angles, pitch and yaw (interchangeable with v), the needle insertion point on any given plane (for example, the guiding template in brachytherapy or alternatively the front surface of the tissue), and the insertion depth are the parameters to be optimized.

Assuming that the targets are originally located on a straight line, the following iterative algorithm can be used to optimize the insertion parameters.

1) Initialize the parameters by passing a line $p^1 + \alpha v^1$ through the targets in the undeformed configuration. The insertion point p_s^1 is the intersection of this line and a desired plane (the front surface of the tissue in this paper). The insertion depth is the distance between the insertion point and the distal target. The parameters p_s and v at the first iteration are shown in Fig. 5(a).
2) Simulate the needle insertion with the given needle heading parameters. The simulation program yields the position of the targets ($u_i^k = \mathcal{F}_i(p_s^k, v^k, d^k), i = 1, \ldots, N$) in the deformed configuration. The superscript k is the index of the iteration. This step is illustrated in Figs. 5(b) and (c).
3) Find the new insertion line parameters (v^{k+1} and p^{k+1}) by fitting a line through the target positions in the deformed configuration [see Figs. 5(b) and (c)].
4) Find the new insertion point p_s^{k+1} as the intersection of this line and the desired plane.
5) Find the new insertion depth d^{k+1} as the distance between p_s^{k+1} and the closest point along the insertion line to the distal target.
6) If the convergence criterion is met, then terminate the algorithm. Otherwise go to step 2.

In Step 1, the line is trivial to compute assuming no tissue deformation. The new line parameters in Step 3 can be calculated by optimizing the line parameters p^{k+1} and v^{k+1} to minimize the sum of distances between the displaced targets and the line.

Therefore

$$(p^{k+1}, v^{k+1}) = \arg\min_{p,v} \left(\sum_{i=1}^{N} \min_{\alpha} \|p + \alpha v - u_i^k\|^2 \right)$$

$$\text{subject to} \quad \|v\| = 1. \tag{3}$$

It is shown in Appendix A that

$$p^{k+1} = \frac{1}{N} \sum_{i=1}^{N} u_i^k \tag{4}$$

and v^{k+1} is the right singular vector corresponding to the largest singular value of $\mathbf{A}$, where

$$\mathbf{A} = \begin{bmatrix} u_1^k - p^{k+1} & u_2^k - p^{k+1} & \cdots & u_N^k - p^{k+1} \end{bmatrix}' \tag{5}$$

and $(\cdot)'$ denotes the transpose of the operand. The convergence criterion used is the satisfaction of a bound on the sum of distances between the needle and the targets in the deformed tissue. In general, due to tissue deformation and target displacement, the targets will not lie on a straight line after needle insertion. Therefore, the aforementioned convergence criterion usually does not converge to zero. Alternatively, the Euclidean norm of differences in the vector of optimization parameters can be considered as a convergence criterion. With this convergence criterion, if the norm of the difference between two consecutive vectors of parameters is smaller than a threshold, the algorithm is terminated [see Fig. 5(d)]. The thresholds in the aforesaid criteria can be determined by experience to match actual geometrical parameters. For example, there is no need to drive the targeting error to less than the needle diameter or the parameter convergence to less than the robot resolution. In fact, organ registration errors are more likely to determine the actual thresholds used in practice.

Using this convergence criteria, the optimization and simulation program can be seen as a single function in which the insertion parameters at iteration k are the inputs and the insertion parameters at iteration $k + 1$ are the outputs. The goal is to find a fixed point of this function.

IV. PERFORMANCE IN SIMULATION

To demonstrate the feasibility of the optimization algorithm, extensive simulations were carried out. The optimization method was implemented in a brachytherapy simulator to reduce the targeting errors caused by deformation. A simplified mesh of the prostate and surrounding tissue [3], [14]—shown in Fig. 3—is used in the simulations. For simplicity, it is assumed that the surrounding tissue is homogeneous.

Insertion of a rigid needle into the 3-D tissue model is simulated using an FEM-based model in a quasi-static mode. The needle is modeled as a straight line without thickness. The needle–tissue interaction is described by a stick–slip force model as in [13] due to its simplicity of implementation and computational speed. In this model, a node is stuck to the needle as long as its reaction force is smaller than a predefined threshold. In this state, three displacement boundary conditions are applied to the stuck node. If the reaction force is greater than the threshold, the node state changes to slip mode. In this state, the node can

slide along the needle. A force boundary condition is applied to this node in the needle axial direction. To confine the node movement to be along the needle, two displacement boundary conditions are applied orthogonally to the needle axis.

A mesh adaptation algorithm [13], [14] is used to increase the accuracy of the simulation. In this method, when the needle tip arrives at a new element boundary, the closest node to the needle tip is relocated on the tip. To do so, the undeformed mesh is adapted in such a way that at the last deformed configuration the corresponding node position coincides with the needle tip. No external force is applied to relocate the node. Mesh adaptation does not lead to inverted elements since the modification is applied to the reference mesh. The stiffness matrix is regenerated accordingly. When using linear FEM, the inverse stiffness matrix can be modified directly, with low computational cost. More details about mesh adaptation algorithm and low-cost inverse stiffness matrix modification are available in [13] and [14].

During the insertion simulation, the displaced location of the targets are of interest and should be computed. Therefore, it is sufficient to compute the displacement of the nodes in contact with the needle and the nodes at the vertices of elements in which the targets are located. When linear FEM is used, this computational shortcut called condensation can be exploited to increase the simulation speed significantly [13]. In this case, the constant global stiffness matrix can be precomputed, inverted and saved in the memory. During the simulation, only a small part of the inverse stiffness matrix that corresponds to the nodes of interest—the operating matrix—is engaged in the calculations [13], [14]. However, in nonlinear FEM, which leads to a nonlinear set of algebraic equations, the displacements of all nodes should be computed at each iteration.

V. SIMULATION RESULTS

Nine sets of targets were assumed inside the prostate model, each of which consisted of three targets located along the z-axis—inspired by the location of the targets in brachytherapy. In each set, the targets were located at depth $z = 15$, $z = 25$, and $z = 35$ mm in the undeformed tissue [see, for example, Fig. 5(a)]. The x–y coordinates of the target sets are shown in Fig. 4 as a cross section of the prostate at $z = 25$ mm.

Although the organs surrounding the prostate are known with good detail from MRI or anatomy literature, the boundary condition of the prostate in the tissue is not accurately known. This is due to the fact that the interaction of the prostate with the surrounding organs during the deformation is not well known and depends on how firmly or loosely it is attached to the surrounding tissue. Other factors such as bladder filling can affect the movement of the prostate and impose complicated boundary conditions. However, the prostate is more stiffly anchored around the pubic arch, and therefore, rotates during needle insertion due to needle torques about the anchor region. To model this, a number of prostate mesh nodes in the anterior/superior region are fixed, and therefore, determine displacement boundary conditions as marked in Fig. 3. Different boundary conditions can lead to different simulation results, and consequently, to
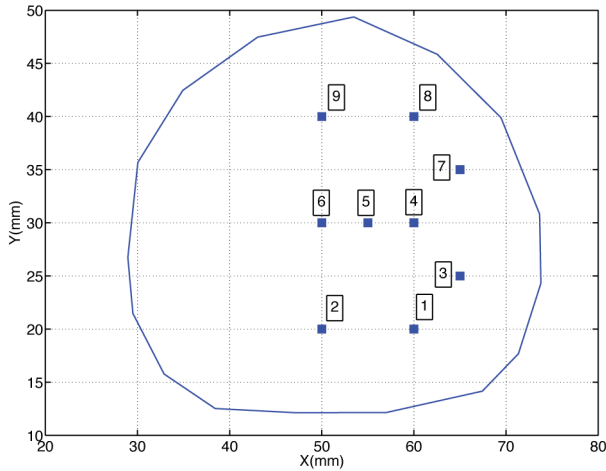
Fig. 4. x–y position of the target sets in a cross section of the prostate at $z = 25$ mm.

TABLE I
SIMULATION PARAMETERS FOR PROSTATE MODEL

(E, ν) for the prostate tissue	(60 kPa, 0.49)
(E, ν) for the surrounding tissue	(20 kPa, 0.49)
Number of Nodes	570
Number of Elements	2801
Element Type	Tetrahedron
Simulation type	Linear strain, quasi-static
Material Type	Linear elastic

different optimized parameters. The optimization algorithm is tested for different boundary condition assumptions and tissue models. The tissue elastic parameters—the Young's modulus E and the Poisson's ratio ν—were typical of soft tissue [31] and are presented, together with other simulation parameters, in Table I.

A. Posterior Surface Fixed

In this case, in addition to nodes in connection with the pubic arch, the nodes located at the back of the mesh are fixed. Therefore, the prostate motion is confined, and hence, one can expect small rotation of the prostate.

The parameter optimization was performed for each of the target sets. The iteration was continued until the change in the vector of optimization parameters was less than 1% or the error—defined as the sum of distances between the needle and the targets—was less than the brachytherapy needle diameter. The linear FEM was used for the simulation. The errors in the first and last iterations, the number of iterations, and the optimized parameters are reported in Table II for each target set. It can be seen that the algorithm converged to submillimeter errors in two iterations for all the target sets. This is due to the small rotations of the prostate caused by the confined boundary conditions.

B. Superior Surface Fixed

In the second boundary condition scenario, the posterior mesh nodes are free while the nodes located on the top of the mesh are fixed. The simulation is performed with the same elastic param-

eters as in the former case. Simulation results are summarized in Table III.

In the two simulated boundary condition scenarios, the tissue is confined and it cannot easily rotate or displace. Therefore, the optimal insertion parameters are close to the initial values, especially for the targets close to the pubic bone where the tissue is more confined (e.g., target sets 8 and 9).

C. Pubic Arch Boundary Condition Only

In another case, the posterior and superior surfaces of the mesh are both free and the prostate is only confined in the area of the pubic arch. In this case, the prostate is able to rotate and deform more than in the two former cases. Therefore, the number of iterations necessary for the optimization algorithm convergence increased. Also, the optimized insertion parameters are considerably different from the initial insertion parameters. However, for target sets 8 and 9, the rotation and consequent displacements are low, since these target sets are close to the center of rotation, and therefore, needle forces produce less torque for these targets compared to targets farther from the center of rotation. The simulation results are summarized in Table IV. The optimization algorithm takes two to five iterations to converge to submillimeter errors.

D. Lower Young's Modulus for the Inclusion

To allow the prostate to deform even more, the elastic modulus of the inclusion is decreased to $E = 40$ kPa to represent a softer tissue. The prostate is only fixed at the connection with the pubic bone. The simulation results in this case are summarized in Table V.

The optimization method shows stability and successful decrease in the targeting error in a maximum of seven iterations. As an example, the optimization steps for the 5th target set in this case are shown in Fig. 5. Fig. 5(a) shows the position of the targets in the undeformed configuration inside the prostate. The first candidate for the insertion line is shown as the line passing through the targets. Figs. 5(b) and (c) show the deformed configuration after the first and the second iterations. The displaced position of the targets, the needle, and the new insertion line are shown in each figure. Fig. 5(d) shows the final iteration in which the targets are very close to the needle and the next insertion path is very close to the old one.

Comparing Tables IV and V shows that in spite of a 33% decrease in the Young's moduli of the prostate in this case, the optimized parameters are not significantly different. Based on this information, one can deduce that optimizing the needle insertion parameters can be helpful even in the presence of uncertainty in the elastic properties of the tissue. Decreasing the Young's modulus and increasing the friction forces have similar effects. Therefore, these cases are not presented here.

E. Neo-Hookean Material Model for Tissue

When the prostate is mainly fixed by the pubic bone only, the tissue can undergo large rotations and deformations. To

TABLE II
SIMULATION RESULTS FOR CASE A

Set	Number of Iterations	1st Iteration Error (mm)	Last Iteration Error (mm)	Optimized angles (yaw, pitch)	Optimized insertion point offset (x, y)	Optimized depth (mm)
1	2	1.8	0.8	(0.5°, 0.4°)	(0.7, -0.2)	56.4
2	2	1.6	0.4	(0.1°, 0.6°)	(0.1, -0.6)	56.3
3	2	1.8	0.5	(0.2°, 1.3°)	(-0.2, -1.1)	56.4
4	2	1.8	0.5	(0.1°, 0.4°)	(0.1, -0.4)	56.4
5	2	1.9	0.3	(0.1°, 0.1°)	(-0.2, -0.1)	56.3
6	2	1.4	0.2	(0.2°, 0.8°)	(0.2, -0.7)	56.1
7	2	1.4	0.4	(0.3°, 0.0°)	(0.3, 0.0)	56.2
8	2	1.4	0.4	(0.5°, 0.0°)	(0.4, 0.0)	56.2
9	2	1.1	0.1	(0.0°, 0.2°)	(0.1, -0.1)	55.6

Posterior mesh surface is fixed.

TABLE III
SIMULATION RESULTS FOR CASE B

Set	Number of Iterations	1st Iteration Error (mm)	Last Iteration Error (mm)	Optimized angles (yaw, pitch)	Optimized insertion point offset (x, y)	Optimized depth (mm)
1	2	5.0	0.7	(1.8°, 1.9°)	(1.2, -1.1)	59.6
2	2	4.2	0.4	(0.3°, 2.4°)	(0.3, -1.7)	59.2
3	2	5.0	0.6	(1.9°, 2.7°)	(0.5, -2.1)	59.8
4	2	3.5	0.7	(1.5°, 1.3°)	(0.9, -0.9)	58.5
5	2	3.1	0.7	(0.9°, 0.9°)	(0.4, -0.5)	58.1
6	2	2.8	0.4	(0.3°, 1.3°)	(0.1, -0.9)	57.6
7	2	3.4	0.5	(2.0°, 0.6°)	(1.2, -0.5)	58.2
8	2	2.9	0.3	(1.3°, 0.3°)	(0.8, -0.2)	57.4
9	2	1.7	0.2	(0.0°, 0.3°)	(0.1, -0.1)	56.5

Superior mesh surface is fixed.

TABLE IV
SIMULATION RESULTS FOR CASE C

Set	Number of Iterations	1st Iteration Error (mm)	Last Iteration Error (mm)	Optimized angles (yaw, pitch)	Optimized insertion point offset (x, y)	Optimized depth (mm)
1	3	13.5	0.6	(3.6°, 9.8°)	(2.6, -5.8)	64.6
2	5	11.3	0.9	(0.9°, 10.7°)	(0.7, -6.8)	65.4
3	3	12.3	0.7	(4.9°, 9.3°)	(3.3, -5.6)	64.6
4	3	8.0	0.5	(4.3°, 6.6°)	(2.6, -4.1)	61.3
5	3	7.1	0.3	(3.2°, 6.5°)	(1.8, -3.9)	60.4
6	3	6.0	0.4	(0.9°, 6.0°)	(0.6, -3.7)	59.5
7	3	7.4	0.4	(6.3°, 3.9°)	(3.8, -2.0)	59.8
8	2	4.4	0.9	(4.3°, 1.8°)	(2.6, -1.1)	58.7
9	2	2.4	0.5	(0.5°, 2.5°)	(0.4, -1.5)	56.9

The tissue is fixed only anteriorly near the pubic arch. $E = 60$ kPa.

TABLE V
SIMULATION RESULTS FOR CASE D

Set	Number of Iterations	1st Iteration Error (mm)	Last Iteration Error (mm)	Optimized angles (yaw, pitch)	Optimized insertion point offset (x, y)	Optimized depth (mm)
1	3	15.7	0.7	(3.9°, 10.6°)	(2.8, -6.3)	66.1
2	7	13.3	1.1	(1.1°, 11.6°)	(0.8, -7.4)	65.6
3	4	13.5	0.7	(5.0°, 10.4°)	(3.3, -6.4)	65.9
4	4	9.6	0.5	(4.7°, 7.4°)	(2.7, -4.4)	60.7
5	3	8.9	0.6	(3.7°, 6.9°)	(2.0, -1.5)	61.7
6	3	5.8	0.6	(0.8°, 5.9°)	(0.6, -3.6)	58.4
7	3	8.7	0.7	(6.8°, 3.4°)	(4.2, -1.8)	61.8
8	3	5.1	0.9	(4.9°, 1.8°)	(3.0, -1.0)	59.5
9	2	2.9	0.6	(0.5°, 2.7°)	(0.4, -1.6)	57.5

The tissue is fixed only anteriorly near the pubic arch. $E = 40$ kPa.

simulate these conditions more accurately, a nonlinear FEM-based model that can accommodate both the geometric and mechanical nonlinearities is used. Neo-Hookean hyperelastic material models [32] are assumed for the prostate and the surrounding tissue. Neo-Hookean material models were previously used to simulate tissue during needle insertion [33]. They have been used also for tissue modeling for liver simulation [34] and brain image registration [35]. Lamé parameters (λ and μ) are usually used in constitutive equations for neo-Hookean material models (please see Appendix B). The material property parameters for the prostate model are $E = 60$ kPa for the inclusion and $E = 20$ kPa for the surrounding tissue ($\nu = 0.49$),
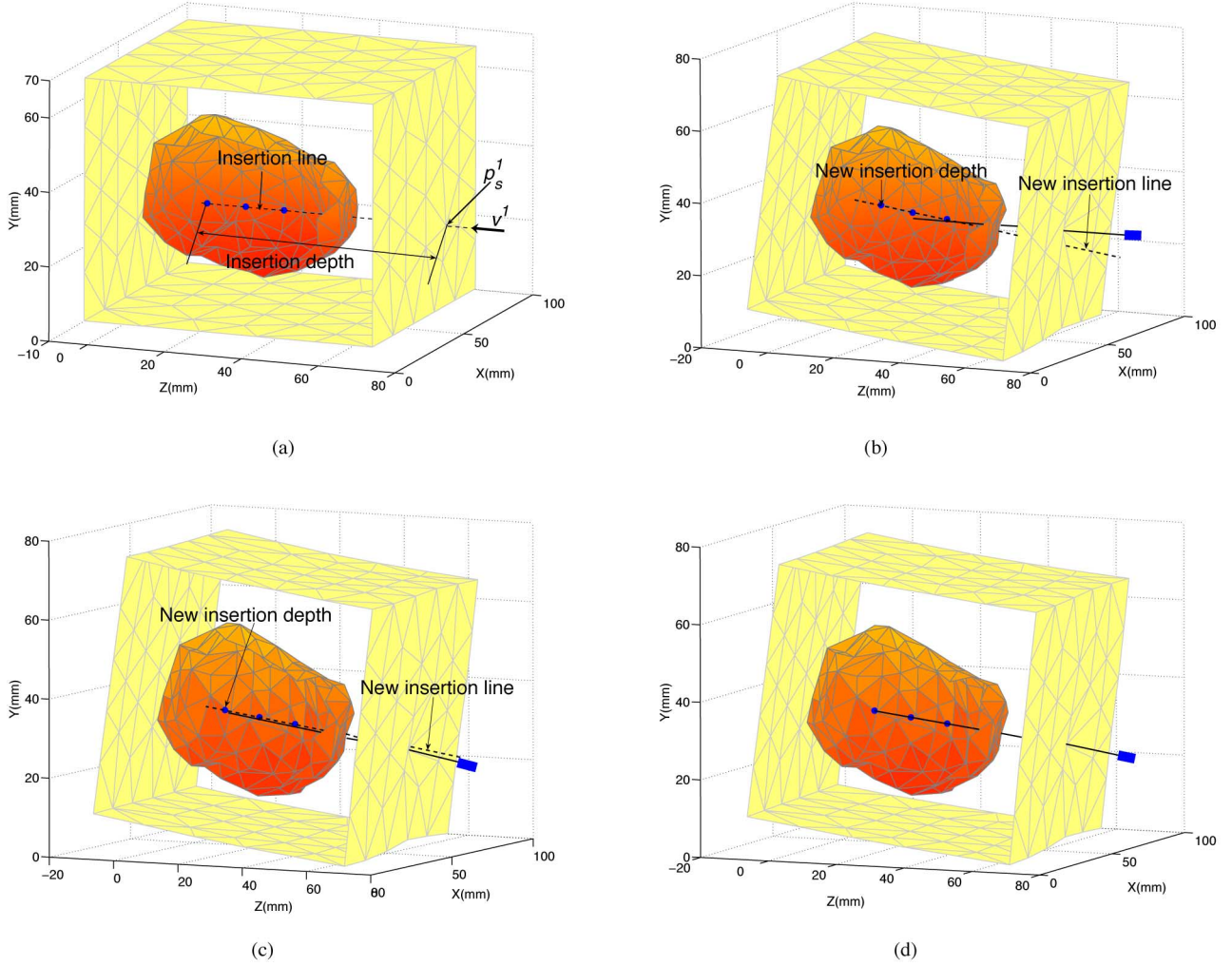
Fig. 5. Simulation iterations for three targets. (a) The undeformed configuration. (b) After the first iteration. (c) After the second iteration. (d) After the third iteration. (b)–(d) show the position of the targets in the deformed tissue after insertion of the needle with the insertion parameters calculated in (a)–(c), respectively. 3-D fitted line is shown as a dotted line. The front surface of the prostate mesh is removed to show the position of the targets and the needle inside.

TABLE VI
SIMULATION RESULTS FOR CASE E

Set	Number of Iterations	1st Iteration Error (mm)	Last Iteration Error (mm)	Optimized angles (yaw, pitch)	Optimized insertion point offset (x, y)	Optimized depth (mm)
1	3	15.5	0.6	(4.3°, 11.0°)	(2.9, -6.3)	64.5
2	4	12.1	0.8	(1.0°, 11.7°)	(0.2, -7.0)	64.8
3	6	13.0	0.4	(5.6°, 10.1°)	(3.5, -6.0)	64.0
4	3	7.4	0.7	(4.6°, 6.7°)	(2.6, -3.9)	61.0
5	3	7.5	0.8	(2.9°, 7.8°)	(1.9, -4.1)	59.4
6	3	6.3	0.6	(0.9°, 6.2°)	(0.7, -3.7)	59.3
7	3	7.8	0.3	(6.1°, 4.2°)	(3.6, -2.3)	60.5
8	3	4.4	0.7	(4.2°, 1.8°)	(2.5, -1.1)	58.6
9	3	2.4	0.5	(0.4°, 2.3°)	(0.4, -1.4)	56.9

Neo-Hookean material model.

corresponding to $\lambda = 985.6$ kPa and $\mu = 20.1$ kPa for the inclusion and $\lambda = 328.8$ kPa and $\mu = 6.7$ kPa for the surroundings. The Newton–Raphson iterative method [32] is used to solve the nonlinear set of algebraic equations. Due to the nonlinearity of the problem, precomputation and condensation cannot be used and the displacement of all the nodes should be computed at each iteration. The optimization is performed for all the nine target sets and the results are summarized in Table VI. The optimization algorithm converged in three to six iterations to submillimeter errors.

VI. EXPERIMENTAL VALIDATION

In order to experimentally validate the optimization algorithm, a prostate phantom was constructed. The tissue phantom
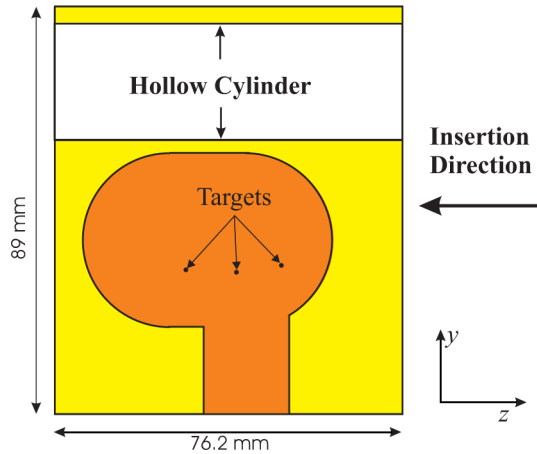
Fig. 6. Cross-section of the phantom designed for the experiment, showing the inclusion, its connective cylinder, the hollow cylinder, and the positions of the targets.
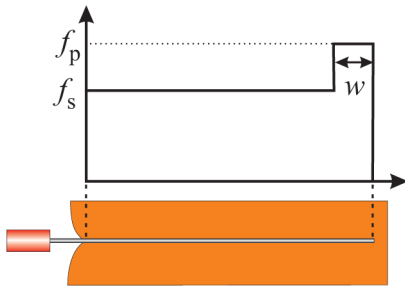

Fig. 8. 3-D mesh of the tissue phantom used in the simulations.

Fig. 7. Force model identified for needle–tissue interaction.

is composed of a prostate mimicking inclusion made of a mixture of PVC plasticizer and plastic hardener surrounded by a substrate made of a mixture of PVC plasticizer and plastic softener. The inclusion consists of a cylinder with two hemispheres at its ends, connected to the base of the phantom with another cylinder of the same material. The combination of the inclusion and its connective cylinder mimics the prostate and its rotation around the pubic bone. A hollow cylinder was provided in the phantom to simulate the rectum. A cross section of the tissue phantom is shown in Fig. 6. The PVC was chosen over bovine gels and agar phantoms because it produces insertion forces that are of the same order of magnitude as the insertion force during prostate brachytherapy, as reported in [29].

In order to identify the parameters required for simulation of needle insertion into this tissue phantom a pilot insertion was executed. An 18-gauge brachytherapy needle (Bard, GA) was inserted into the tissue phantom with a constant speed, while the tissue phantom was imaged using the sagittal (axial) array of a TRUS probe housed in the hollow cylinder provided in the tissue phantom. The sequence of recorded RF signals was later used to measure tissue displacement during needle insertion [36]. The insertion forces and needle positions were also measured. Using the method described in [27] and [36] the parameters of a three-parameter force distribution model (see Fig. 7) and the elasticity modulus were identified for each layer of the tissue by incorporating the force–displacement data gathered during the
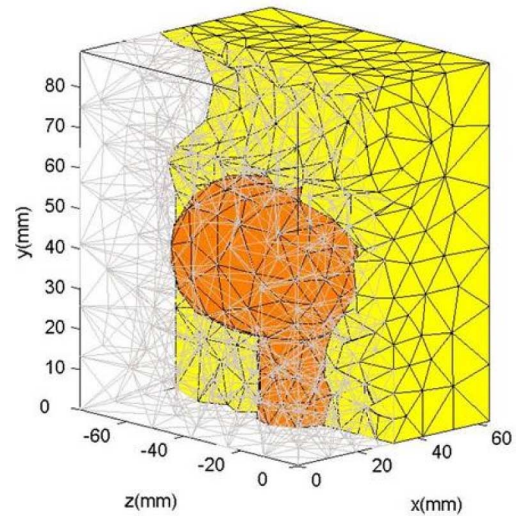
experiment. The three-parameter force model consists of a peak force density f_p contributing to cutting, shaft force density f_s contributing to friction, and the width of the peak force density w as shown in Fig. 7. Using the identified force model and the elastic moduli, a linear FEM-based simulator was constructed to simulate the needle insertion into the tissue phantom (for more details see [27] and [36]). The 3-D mesh of the phantom is shown in Fig. 8 and the simulation parameters are presented in Table VII. The simulation was implemented in quasi-static mode. The bottom side of the tissue phantom was fixed using a wire-mesh and was assumed to be the fixed displacement boundary condition in the simulation. The needle was assumed rigid and without thickness.

A 6-DOF position stage was used to orient and insert the needle into the tissue phantom. The stage consists of two perpendicular manually adjustable rotational stages to orient the needle, connected to a manually adjustable linear stage with three degrees of freedom to localize the needle tip on the tissue surface. The sixth degree of freedom is a motorized linear stage to insert the needle to the desired depth with constant speed. The stage is shown in Fig. 9.

Three targets were located inside the tissue phantom in the central sagittal plane ($x = 31.8$ mm). To create the targets, a needle was inserted into the phantom from three points on its side. The intersections of needle tracks and the central sagittal plane were assumed to be the targets. The position of the targets are shown in Fig. 6. Since the targets were manually created, they were not located on a straight line. The needle insertion parameters were optimized using the proposed algorithm for these three targets. The needle was inserted twice at the same speed of 5 mm/s, once with the initial insertion parameters and another time with the optimized ones. Table VIII shows the iterations of the optimization algorithm. The insertion parameters and simulated errors are shown for all the iterations, while the actual errors are reported for the two real insertions. Since the targets are located on the central sagittal plane and the tissue phantom is symmetric, the targets will not move laterally (in

TABLE VII
SIMULATION PARAMETERS FOR PHANTOM

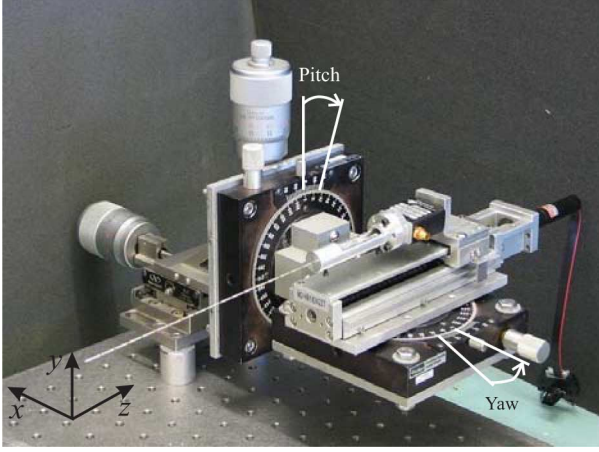|	Young's Modulus kPa	Poisson's ratio	f_s (N/m)	f_p (N/m)	w (mm)
Inclusion	30	0.49	90	380	4.5
Surroundings	7	0.49	50	100	4.0

Fig. 9. The 6-DOF stage used for the positioning and orientation of the needle.

the x-direction) if the needle is inserted in the central sagittal plane (yaw = 0). However, due to the asymmetric mesh used for the simulation, after each insertion of the needle, small lateral displacements were observed resulting in a nonzero yaw angle of insertion for the next iteration. This nonzero yaw angle was assumed as simulation error and was set to zero before advancing to the next iteration. The optimization iterations were terminated, when the error was less than the needle diameter (1.28 mm).

The brachytherapy needle consists of a stylet sliding inside a cannula. The stylet is used to push the seeds out of the needle after the insertion of the needle into tissue. In order to reduce needle bending due to the beveled-tip of the needle, the needle stylet was fully inserted into the cannula to create a symmetric tip for the needle. No significant needle bending was observed. The TRUS probe which was used in the pilot study was removed before insertions. After the needle was retracted, the tissue phantom was imaged using a hand-held ultrasound probe. Fig. 10 shows the position of the targets and the track of the needle. These figures show that insertion with optimal insertion values decreased the targeting error significantly.

For the simulations used in this part, the three-parameter force model—shown in Fig. 7—was implemented. It was shown that such a model can accurately predict the needle insertion forces and the tissue deformations during insertion of a needle into a two-layered PVC prostate phantom similar to the one used in this paper [27], [36]. The parameters of this model were identified in [36] for the same tissue phantom. In order to implement this force distribution model, at each sample time of the simulation, this force profile should be integrated over the part of the needle that is inside the tissue in the deformed configuration. The resultant force is distributed on the mesh nodes that are located on the needle, based on their relative distances from each other and their distances from the needle tip. These forces are applied as
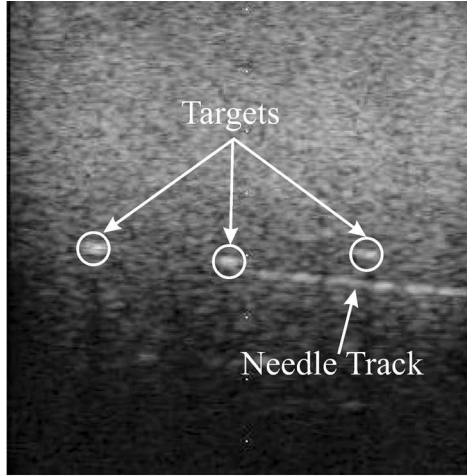
a force boundary condition in the simulation and result in nodal displacements. However, due to tissue deformation, especially at the point of entry of the needle, the length of the part of the needle that is inside the tissue is a function of the displaced nodal positions that are part of the simulation results. Therefore, an iterative method was employed to implement the three-parameter force model in each time sample [27], [36]. In contrast, the stick–slip method can be implemented in a single step for each sample time of the simulation. However, the three-parameter force model delivers higher accuracy in predicting the insertion force and tissue deformation. In general the force recorded during insertion of a needle into a PVC phantom shows a high slope rise at the start of the penetration followed by a more gradual increase as the insertion continues (see, for example, measured insertion forces, reported in [27]). Such a force can be easily modeled by the three-parameter force model. In contrast, upon implementation of the stick–slip model, anytime a node sticks to the needle tip, a displacement boundary condition is applied; thus, the force increases with a gradient that is a function of the elastic properties of the tissue. When the node state changes to slip mode, the force gradient is a function of the friction. Therefore, the insertion force that results from the stick–slip model cannot be smooth as the one recorded from a PVC phantom.
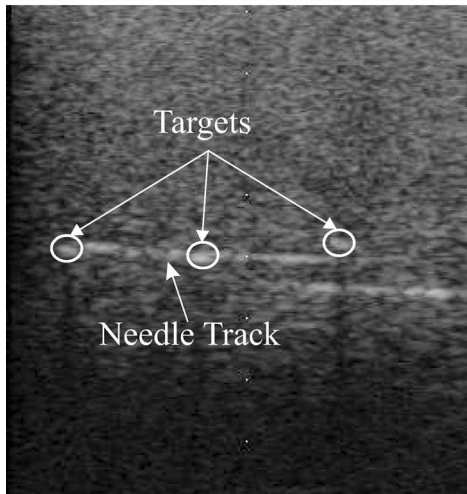
VII. DISCUSSION

For each iteration of the optimization algorithm, a needle insertion process was simulated. When the tissue model was assumed to have a linear elastic behavior, precomputation and accelerated simulation methods were employed to increase the simulation speed. As an example, the original stiffness matrix for the prostate model was of dimensions 1710×1710 which was inverted and saved in the memory. However, only a part of the inverted stiffness matrix (operating matrix) was used when the tissue was assumed to be linear elastic. In this paper, the operating matrix dimension was 30×30 at the maximum penetration of the needle and maximum 50×50 at the final iteration to find the displaced locations of the targets. Fast update algorithms from [14] and [13] were used to implement the mesh adaptation and update the inverted stiffness matrix. However, the adaptation process is time-consuming due to the large dimensions of the original matrix and huge number of multiplications necessary to update the inverted stiffness matrix. The simulation part was programmed in MATLAB and the mean time per simulation was 50 s. The mesh adaptation algorithm, the application of force and displacement boundary conditions, and the change of coordinate system from global to needle coordinate system are included in each simulation. The time per simulation is the time necessary to simulate insertion of a needle to a desired depth. Since variable insertion depths were simulated in this study, the mean time per simulation was reported. With implementation of the code in C++ as in [14], higher speeds

TABLE VIII
OPTIMIZATION STEPS FOR INSERTION INTO TISSUE PHANTOM, SIMULATED AND MEASURED ERRORS

Iteration Number	Angles (Yaw,Pitch)	Insertion point (x, y)	Insertion depth (mm)	Simulated error (mm)	Real error (mm)
1	$(0°, 2.5°)$	(31.8,33.5)	47.7	10.0	13.5
2	$(0°, 3.9°)$	(31.8,34.3)	55.7	3.3	–
3	$(0°, 3.9°)$	(31.8,34.6)	58.1	1.6	–
4	$(0°, 4.0°)$	(31.8,34.9)	58.8	1.2	1.7

(a)

(b)

Fig. 10. Experimental results. The target positions and the needle tracks inserted (a) without optimization and (b) with optimized parameters. The images are brightened and cropped for better visibility.

can be achieved. For more details about computational issues in needle insertion simulation, please refer to [13] and [14]. In the simulation with prostate model, the stick–slip interaction model was used. However, in the tissue phantom simulation, the three-parameter force model was implemented. As discussed in Section VI, implementation of this model needs several iterations for each time sample, and therefore, requires significantly more computational time. The original stiffness matrix in this case was of dimensions 2361×2361.

With a nonlinear system, it is not possible to use the precomputation methods. A linear set of equations that resulted from Newton–Raphson should be solved at each iteration the coefficient matrix of which—named tangent stiffness matrix—is a function of displacements in all the nodes. Therefore, a set of algebraic equations with matrix of dimensions 1710×1710 was solved at each iteration for each sample time of the simulation. The Newton–Raphson method never showed instability in our simulations and always converged to the desired errors within less than ten iterations, while convergence was achieved in five iterations in most simulations. The mean time per simulation was 70 minutes using MATLAB. The tangent stiffness matrix is sparse. Therefore, sparse matrix calculation methods can be exploited to increase the simulation speed. In addition, a computationally efficient method for simulation of needle insertion into neo-Hookean tissue models was introduced in [33]. However, linear models are always faster.

In Section V-C and V-E, the tissue parameters and the boundary conditions are similar while the simulation method is different. Since the tissue was only anchored around the pubic bone and the rotation was high, one can expect the largest difference between linear and nonlinear models. However, a comparison between Tables IV and VI shows only minor differences between optimal parameters obtained from linear and nonlinear models. Therefore, when very high accuracy is not required, linear models can be used instead of nonlinear ones due to their significantly higher speed.

The optimization method showed convergence in a few iterations in all the simulation cases. When the simulation model was linear, the error was monotonically decreasing in each iteration. The optimization error at each iteration for the linear simulation model is shown in Figs. 11(a) and (b). In these figures, the prostate mesh was anchored around the pubic bone only. Using the nonlinear model, the error monotonically decreased in all the cases except for sample targets in set 3. The error in optimization for the nonlinear simulation model is shown in Fig. 11(c).

The boundary conditions applied in the simulations are not realistic. However, they cover a wide range of possible boundary conditions, from confined situation as in Sections V-A and V-B to free to rotate situation as in Sections V-C to V-E. The optimization algorithm was stable in all cases. Note that it is possible to stabilize such a fixed-point algorithm—should an instability occur—by switching between the proposed iteration and a gradient-based descent, as done to stabilize Newton's method.

It should be noted that Lagerburg *et al.* [1] measured prostate rotations of maximum $13.8°$ in the coronal plane and rotations between $-8.5°$ and $10.2°$ in the sagittal plane. The rotation in
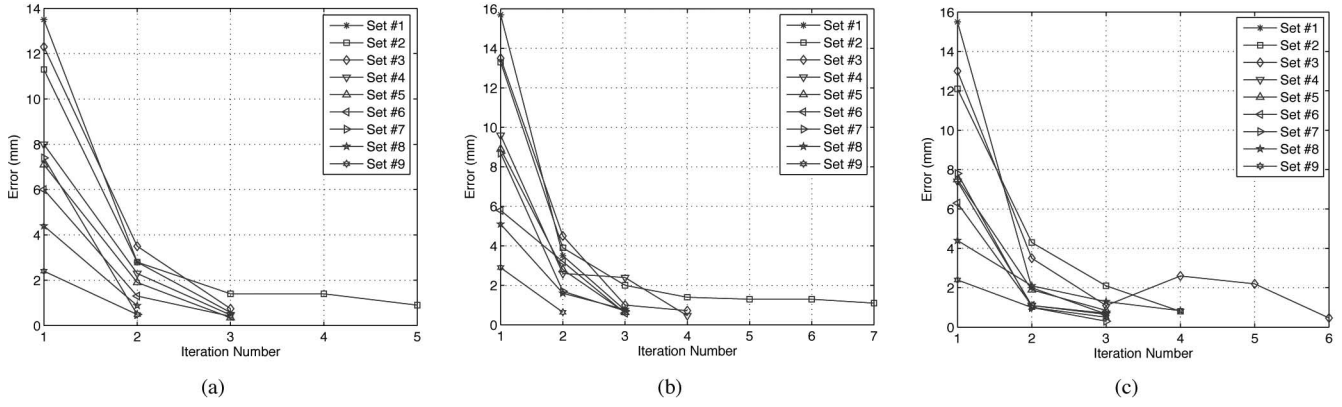
Fig. 11.   Optimization error in different iterations. (a) Linear model with $E = 60$ kPa. (b) Linear model with $E = 40$ kPa. (c) Neo-Hookean nonlinear model. The boundary conditions are the fixed points in connection with the pubic bone.

coronal plane showed strong correlation to the needle insertion point and the method of insertion (with or without locking needles), while the rotation in the sagittal plane did not show significant correlation with the insertion point [1]. The extent of rotations in the simulations reported in this paper shows the most resemblance to the ones reported in [1], when the prostate is only anchored around the pubic bone. However, the simulated rotations in the sagittal plane are strongly correlated with the insertion point of the needle and negative values for rotations in this plane are impossible. Therefore, prior to clinical use of the optimization algorithm, accurate boundary conditions of the prostate within the tissue should be determined as the boundary conditions play a significant role in the outcomes of the optimization. In addition, the elastic properties of the prostate and the surrounding tissue should be identified. MRI does produce anatomical detail of the prostate region with very good detail and could be used to produce the required boundary conditions for our simulations. It can also be used to generate a mesh of the prostate and surrounding organs with more details. Alternatively, elastography is also being explored for such modeling as it can produce both the boundary conditions and the tissue elasticity parameters effectively [37], [38].

The proposed optimization algorithm was combined with FEM simulation methods in this work. Two different needle–tissue interaction models were employed in these simulations. Since the simulation and optimization parts are independent and the assumptions in the simulation part do not put any restriction on the optimization algorithm, the optimization approach can be combined with any simulation method. In addition, similar methodology can be exploited for other medical interventions involving needle insertion.

The needle was assumed to be rigid and straight. In the experiment, the needle stylet was fully extended to create a symmetric tip. Needle bending was negligible even though the needle was flexible. Common brachytherapy needles are flexible and beveled-tip, and may bend due to the bevel force. However, a symmetric-tip needle can be used, or alternatively, the needle can be rotated during insertion as it has been shown to significantly decrease the needle bending due to bevel forces [39]. Under these assumptions, a rigid needle model can be used for

insertion optimization. In addition, the optimized parameters can also be used as a starting insertion point for flexible needle steering methods such as those presented in [22] or [23]. At first, the initial position of the needle tip and needle orientation can be optimized using the presented algorithm assuming rigidity of the needle. Later the needle can be steered during penetration to further decrease the errors. The modeling and simulation of the beveled-tip effect on a brachytherapy needle path is part of the future research.

VIII. CONCLUSIONS AND FUTURE WORK

An approach to the optimization of needle insertion point, heading, and depth was proposed for the planning of needle insertions into deformable tissue. The approach was demonstrated in a number of simulations that have explored the effect of boundary conditions, elasticity parameters, and nonlinearity on optimization performance. Unlike in previously published work, this approach employs a fixed-point type of iteration instead of descent or search methods, and therefore, works faster. In fact, more simulation iterations are required in a single step of a descent method than are required to attain good convergence in almost all the simulations studied. The simulation was performed using an FEM-based model in quasi-static mode. The algorithm converged to submillimeter errors in few iterations in all the cases.

The optimization method was also validated in an experiment on a two-layered prostate phantom. The insertion parameters were optimized for three targets inside the phantom. The needle was inserted using a 6-DOF mechanical system. The mechanical system had five manually adjustable DOFs to orient the needle and localize the tip and a motorized linear stage to insert the needle with desired speed. The experiment showed substantial decrease in the targeting error.

In the future, the optimization algorithm will be applied to a more realistic model of the prostate based on segmented patient images that include boundary conditions such as the pubic bone and the bladder. We will include more accurate needle models accounting for needle flexibility and lateral bevel forces.

APPENDIX A

3-D LINE FITTING TO DISPLACED TARGETS

The optimization problem to be solved to fit a 3-D line to some targets is presented in (3). The optimization problem in (3) includes a minimization problem over the parameter α for each displaced target $u_i^k, i = 1, \ldots, N$. Let

$$q_i = \min_\alpha J_i = \min_\alpha \|p + \alpha v - u_i^k\|^2$$

$$\text{subject to:} \quad \|v\| = 1, i = 1, \ldots, N. \quad (6)$$

Taking the derivative of J_i with respect to α, we have

$$\frac{\partial J_i}{\partial \alpha} = 2\alpha v'v - 2v'(u_i^k - p) = 0 \Rightarrow \alpha = v'(u_i^k - p). \quad (7)$$

Substituting for α in (6), we have

$$q_i = \|(I - vv')(u_i^k - p)\|^2 \quad (8)$$

where I is a 3×3 identity matrix.

Substituting (8) into (3), we have

$$(p^{k+1}, v^{k+1}) = \arg\min_{p,v} \sum_{i=1}^{N} \|(I - vv')(u_i^k - p)\|^2$$

$$\text{subject to} \quad \|v\| = 1. \quad (9)$$

Please note that $(I - vv')(u_i^k - p)$ is the normal projection of the vector $(u_i^k - p)$ on the vector v. By changing the constrained optimization problem to an unconstrained one, taking the derivative of the new cost function with respect to p, and equating it to zero, we have

$$-2(I - vv')'(I - vv') \sum_{i=1}^{N} (u_i^k - p^{k+1}) = 0 \Rightarrow$$

$$p^{k+1} = \frac{1}{N} \sum_{i=1}^{N} u_i^k. \quad (10)$$

Now that p^{k+1} is known, the optimization problem can be changed to finding the optimal line—parameterized by v—that passes through p^{k+1} and has the minimized accumulated distances to the displaced targets. Since p^{k+1} and u_i^k are known and constant, the problem changes to minimization of the accumulated magnitudes of the normal projections of $u_i^k - p^{k+1}, i = 1, \ldots, N$ to the prospective unit vector v. This minimization problem can be exchanged with the problem of maximization of the accumulated magnitudes of the parallel projections of $u_i^k - p^{k+1}, i = 1, \ldots, N$ on the unit vector v. Therefore

$$v^{k+1} = \arg\max_v \sum_{i=1}^{N} \left((u_i^k - p^{k+1})'v\right)^2 = \arg\max_v \|\mathbf{A}v\|^2$$

$$\text{subject to:} \quad \|v\| = 1 \quad (11)$$

where $\mathbf{A}$ is defined in (5). The right side of the (11) is the singular value problem, and therefore, v^{k+1} is the right singular vector of $\mathbf{A}$ corresponding to its largest singular value.

APPENDIX B

NEO-HOOKEAN HYPERELASTIC MATERIAL MODEL

The stored energy density for a neo-Hookean material that includes the compressibility effect is expressed as [32]

$$W(\mathcal{I}, \mathcal{J}) = \frac{1}{2}\mu (\mathcal{I} - 3 - 2\ln\mathcal{J}) + \frac{1}{2}\lambda (\mathcal{J} - 1)^2 \quad (12)$$

where $\mathcal{I}$ is the first invariant of the deformation tensor and $\mathcal{J}$ is the determinant of the deformation gradient tensor. λ and μ are Lamé parameters that are interchangeable with Young's modulus and Poisson's ratio. The Green strain, the second Piola–Kirchhoff stress, and the material moduli tensors with respect to the reference configuration can be written as

$$\epsilon_{ij} = \frac{1}{2}(C_{ij} - \delta_{ij}) \quad (13)$$

$$\sigma_{ij} = \mu \left(\delta_{ij} - C_{ij}^{-1}\right) + \lambda\mathcal{J} \left(\mathcal{J} - 1\right) C_{ij}^{-1} \quad (14)$$

$$D_{ijkl} = \lambda\mathcal{J} \left(2\mathcal{J} - 1\right) C_{ij}^{-1} C_{kl}^{-1} + 2 \left[\mu - \lambda\mathcal{J} \left(\mathcal{J} - 1\right)\right] \mathcal{C}_{ijkl}^{-1} \quad (15)$$

where $i, j, k, l \in \{1, 2, 3\}$, δ_{ij} is Kronecker delta, C is the right Cauchy–Green deformation tensor, C_{ij}^{-1} is the element (i, j) of C^{-1}, and

$$\mathcal{C}_{ijkl}^{-1} = \frac{1}{2}[C_{ik}^{-1}C_{jl}^{-1} + C_{il}^{-1}C_{jk}^{-1}]. \quad (16)$$

Discretization and approximation of these equations over several finite elements lead to a set of nonlinear algebraic equations of the form [32]

$$\Phi(\underline{u}) - \underline{f} = 0 \quad (17)$$

where $\underline{u}$ and $\underline{f}$ are vectors of nodal displacements and external forces, respectively. The Newton–Raphson method is used to iteratively solve the nonlinear equations of deformation [32]. Therefore, the following equation should be solved for $\delta\underline{u}$ at each iteration

$$\mathbf{K_T} (\underline{u}^t)\delta\underline{u}^{t+1} = -(\Phi(\underline{u}^t) - \underline{f}) = -\underline{e}^t \quad (18)$$

where $\mathbf{K_T}$ is the tangent stiffness matrix constructible from (13)–(16), $\underline{u}^t$ is the vector of nodal displacements at iteration t, $\underline{e}^t$ is the error vector, and

$$\underline{u}^{t+1} = \underline{u}^t + \delta\underline{u}^{t+1}. \quad (19)$$

REFERENCES

[1] V. Lagerburg, M. A. Moerland, J. J. Lagendijk, and J. J. Battermann, "Measurement of prostate rotation during insertion of needles for brachytherapy," *Radiother. Oncol.*, vol. 77, no. 3, pp. 318–323, 2005.

[2] R. Taschereau, J. Pouliot, J. Roy, and D. Tremblay, "Seed misplacement and stabilizing needles in transperineal permanent prostate implants," *Radiother. Oncol.*, vol. 55, no. 1, pp. 59–63, 2000.

[3] O. Goksel, S. E. Salcudean, S. P. DiMaio, R. Rohling, and J. Morris, "3D needle-tissue interaction simulation for prostate brachytherapy," in *Proc. Int. Conf. Med. Image Comput. Comput. Assist. Interv.*, 2005, pp. 827–834.

[4] V. Lagerburg, M. A. Moerland, M. van Vulpen, and J. J. Lagendijk, "A new robotic needle insertion method to minimise attendant prostate motion," *Radiother. Oncol.*, vol. 80, no. 1, pp. 73–77, 2006.

[5] G. Fichtinger, E. C. Burdette, A. Tanacs, A. Patriciu, D. Mazilu, L. L. Whitcomb, and D. Stoianovici, "Robotically assisted prostate brachytherapy

with transrectal ultrasound guidance Phantom experiment," *Brachytherapy*, vol. 5, no. 1, pp. 14–26, 2006.

[6] S. P. DiMaio, S. Pieper, K. Chinzei, N. Hata, S. J. Haker, D. F. Kacher, G. Fichtinger, C. M. Tempany, and R. Kikinis, "Robot-assisted needle placement in open MRI: System architecture, integration and validation," *Comput. Aided Surg.*, vol. 12, no. 1, pp. 15–24, 2007.

[7] H. Bassan, T. Hayes, R. Patel, and M. Moallem, "A novel manipulator for 3D ultrasound guided percutaneous needle insertion," in *Proc. IEEE Int. Conf. Robot. Autom.*, 2007, pp. 617–622.

[8] Y. D. Zhang, T. K. Podder, W. S. Ng, J. Sherman, V. Misic, D. Fuller, E. M. Messing, D. J. Rubens, J. G. Strang, R. Brasacchio, and Y. Yu, "Semi-automated needling and seed delivery device for prostate brachytherapy," in *Proc. IEEE/RSJ Int. Conf. Intell. Robots Syst.*, 2006, pp. 1279–1284.

[9] S. E. Salcudean, T. D. Prananta, W. J. Morris, and I. Spadinger, "A robotic needle guide for prostate brachytherapy," in *Proc. IEEE Int. Conf. Robot. Autom.*, 2008, pp. 2975–2981.

[10] R. Alterovitz, K. Goldberg, J. Pouliot, R. Taschereau, and I. C. Hsu, "Sensorless planning for medical needle insertion procedures," in *Proc. IEEE/RSJ Int. Conf. Intell. Robots Syst.*, 2003, vol. 3, pp. 3337–3343.

[11] R. Alterovitz, K. Goldberg, and A. Okamura, "Planning for steerable bevel-tip needle insertion through 2D soft tissue with obstacles," in *Proc. IEEE Int. Conf. Robot. Autom.*, 2005, pp. 1640–1645.

[12] N. Abolhassani, R. Patel, and M. Moallem, "Needle insertion into soft tissue: A survey," *Med. Eng. Phys.*, vol. 29, no. 4, pp. 413–431, 2007.

[13] S. P. DiMaio and S. E. Salcudean, "Needle insertion modeling and simulation," *IEEE Trans. Robot. Autom.: Spec. Issue Med. Robot.*, vol. 19, no. 5, pp. 864–875, Oct. 2003.

[14] O. Goksel, S. E. Salcudean, and S. P. DiMaio, "3D simulation of needle-tissue interaction with application to prostate brachytherapy," *Comput. Aided Surg.*, vol. 11, no. 6, pp. 279–288, 2006.

[15] R. Alterovitz, J. Pouliot, R. Taschereau, I. C. Hsu, and K. Goldberg, "Simulating needle insertion and radioactive seed implantation for prostate brachytherapy," in *Medicine Meets Virtual Reality 11*. J. D. Westwood *et al.*, Eds. IOS Press, 2003, pp. 19–25.

[16] E. Dehghan and S. E. Salcudean, "Needle insertion point and orientation optimization in non-linear tissue with application to brachytherapy," in *Proc. IEEE Int. Conf. Robot. Autom.*, 2007, pp. 2267–2272.

[17] S. Nag, J. P. Ciezki, R. Cormak, S. Doggett, K. Dewyngaert, G. K. Edmundson, R. G. Stock, N. N. Stone, Y. Yan, and M. J. Zelefsky, "Intra-operative planning and evaluation of permanent prostate brachytherapy: Report of the American brachytherapy society," *Int. J. Radiat. Oncol., Biol., Phys.*, vol. 51, no. 5, pp. 1422–1430, 2001.

[18] R. J. Webster, III, J. S. Kim, N. J. Cowan, G. S. Chirikjian, and A. M. Okamura, "Nonholonomic modeling of needle steering," *Int. J. Robot. Res.*, vol. 25, no. 5/6, pp. 509–525, 2006.

[19] R. Alterovitz, A. Lim, K. Goldberg, G. S. Chirikjian, and A. M. Okamura, "Steering flexible needles under Markov motion uncertainty," in *Proc. IEEE/RSJ Int. Conf. Intell. Robots Syst.*, 2005, pp. 1570–1575.

[20] W. Park, J. S. Kim, Y. Zhou, N. J. Cowan, A. M. Okamura, and G. S. Chirikjian, "Diffusion-based motion planning for a nonholonomic flexible needle model," in *Proc. IEEE Int. Conf. Robot. Autom.*, 2005, pp. 4600–4605.

[21] E. Dehghan, O. Goksel, and S. E. Salcudean, "A comparison of needle bending models," in *Proc. Med. Image Comput. Comput. Assist. Interv.*, 2006, pp. 305–312.

[22] S. P. DiMaio and S. E. Salcudean, "Needle steering and motion planning in soft tissues," *IEEE Trans. Biomed. Eng.*, vol. 52, no. 6, pp. 965–974, Jun. 2005.

[23] D. Glozman and M. Shoham, "Flexible needle steering and optimal trajectory planning for percutaneous therapies," in *Proc. Med. Image Comput. Comput. Assist. Interv*. New York: Springer-Verlag, 2004, pp. 137–144.

[24] N. Abolhassani, R. Patel, and M. Moallem, "Trajectory generation for robotic needle insertion in soft tissue," in *Proc. IEEE Eng. Med. Biol. Soc. Int. Conf.*, 2004, pp. 2730–2733.

[25] M. Heverly, P. Dupont, and J. Triedman, "Trajectory optimization for dynamic needle insertion," in *Proc. IEEE Int. Conf. Robot. Autom.*, 2005, pp. 1646–1651.

[26] A. Okamura, C. Simone, and M. O'Leary, "Force modeling for needle insertion into soft tissue," *IEEE Trans. Biomed. Eng.*, vol. 51, no. 10, pp. 1707–1716, Oct. 2004.

[27] E. Dehghan, X. Wen, R. Zahiri-Azar, M. Marchal, and S. E. Salcudean, "Needle-tissue interaction modeling using ultrasound-based motion estimation: Phantom study," *Comput. Aided Surg.*, vol. 13, no. 5, pp. 265–280, 2008.

[28] H. Kataoka, T. Washio, K. Chinzei, K. Mizuhara, C. Simone, and A. Okamura, "Measurement of the tip and friction force acting on a needle during penetration," in *Proc. Med. Image Comput. Comput. Assist. Interv.*, 2002, vol. 2488, pp. 216–223.

[29] T. Podder, D. Clark, J. Sherman, D. Fuller, E. Messing, D. Rubens, J. Strang, R. Brasacchio, L. Liao, W.-S. Ng, and Y. Yu, "In vivo motion and force measurement of surgical needle intervention during prostate brachytherapy," *Med. Phys.*, vol. 33, no. 8, pp. 2915–2922, 2006.

[30] S. P. DiMaio and S. E. Salcudean, "Needle steering and model-based trajectory planning," in *Proc. Med. Image Comput. Comput. Assist. Interv.*, 2003, pp. 33–40.

[31] J. Ophir, S. Alam, B. Garra, F. Kallel, E. Konofagou, T. Krouskop, and T. Varghese, "Elastography: Ultrasonic estimation and imaging of the elastic properties of tissues," *Eng. Med.*, vol. 213, no. 3, pp. 203–233, 1999.

[32] O. C. Zienkiewicz and R. L. Taylor, *The Finite Element Method: Solid Mechanics*, 5th ed. London, U.K.: Butterworth-Heinemann, 2000, vol. 2.

[33] H. W. Nienhuys and A. F. van der Stappen, "A computational technique for interactive needle insertions in 3D nonlinear material," in *Proc. IEEE Int. Conf. Robot. Autom.*, 2004, vol. 2, pp. 2061–2067.

[34] X. Wu, M. S. Downes, T. Goktekin, and F. Tendick, "Adaptive nonlinear finite elements for deformable body simulation using dynamic progressive meshes," *Comput. Graph. Forum*, vol. 20, no. 3, pp. 349–358, 2001.

[35] S. K. Kyriacou and C. Davatzikos, "A biomechanical model of soft tissue deformation, with applications to non-rigid registration of brain images with tumor pathology," in *Proc. Med. Image Comput. Comput. Assist. Interv.*, 1998, pp. 531–538.

[36] E. Dehghan and S. E. Salcudean, "Needle insertion study using ultrasound-based 2D motion tracking," in *Proc. Med. Image Comput. Comput. Assist. Interv.*, 2008, pp. 660–667.

[37] J. Ophir, S. K. Alam, B. S. Garra, F. Kallel, E. E. Konofagou, T. Krouskop, C. R. B. Merritt, R. Righetti, R. Souchon, and S. Srinivasan, T. Varghese, "Elastography: Imaging the elastic properties of soft tissues with ultrasound," *Med. Ultrasonics*, vol. 29, no. 4, pp. 155–171, 2002.

[38] S. E. Salcudean, D. French, S. Bachmann, R. Zahiri-Azar, X. Wen, and W. J. Morris, "Viscoelasticity modeling of the prostate region using vibro-elastography," in *Proc. Med. Image Comput. Comput. Assist. Interv.*, 2006, pp. 389–396.

[39] N. Abolhassani, R. V. Patel, and F. Ayazi, "Minimization of needle deflection in robot-assisted percutaneous therapy," *Int. J. Med. Robot. Comput. Assist. Surg.*, vol. 3, no. 2, pp. 140–148, 2007.

Ehsan Dehghan (S'05) was born in Isfahan, Iran, in 1979. He received the B.Sc. and M.Sc. degrees in electrical engineering from Sharif University of Technology, Tehran, Iran, in 2001 and 2003, respectively. He is currently working toward the Ph.D. degree in electrical and computer engineering at the University of British Columbia, Vancouver, BC, Canada.

His current research interests include computer-aided surgery, medical robotics, surgery and needle insertion simulation, soft tissue modeling, finite-element modeling, and control systems.

Septimiu E. Salcudean (S'78–M'79–SM'03–F'05) received the B.Eng. and M.Eng. degrees from McGill University, Montreal, QC, Canada, and the Ph.D. degree from the University of California, Berkeley, all in electrical engineering.

From 1986 to 1989, he was a Research Staff Member with the Robotics Group, IBM T. J. Watson Research Center. He then joined the Department of Electrical and Computer Engineering, University of British Columbia, Vancouver, BC, Canada, where he is currently a Professor and holds a Canada Research Chair. From 1996 to 1997, he was at French Aeronautics and Space Research Center (ONERA)–Toulouse Research Center (CERT) (aerospace-controls laboratory), Toulouse, France, where he held a Killam Research Fellowship. During 2005, he was with the Medical Robotics Group (GMCAO), Centre National de la Recherche Scientifique (CNRS), Grenoble, France. His current research interests include medical robotics and ultrasound image guidance, elastography, haptic interfaces, and virtual environments.

Prof. Salcudean is a Fellow of the Canadian Academy of Engineering. He has been a co-organizer of several symposia on haptic interfaces and a Technical and Senior Editor of the IEEE TRANSACTIONS ON ROBOTICS AND AUTOMATION.